JOURNAL OF Materials CHEMISTRY

Synthesis and structural investigations of the double perovskites $REBaFe_2O_{5+w}$ (RE = Nd, Sm)

Pavel Karen*[a] and Patrick M. Woodward[b]†

[a]*Department of Chemistry, University of Oslo, P.O. Box 1033 Blindern, 0315 Oslo, Norway. E-mail: pavel.karen@kjemi.uio.no*
[b]*Physics Department, Brookhaven National Laboratory, Upton, NY 11973, USA*

Received 30th November 1998, Accepted 14th December 1998

By selection of appropriately sized rare earth elements and suitable reaction atmosphere, a new double-perovskite-type iron oxide $REBaFe_2O_{5+w}$ (RE = Nd and Sm) has been synthesized, with, ideally, all Fe atoms in square-pyramidal coordinations when $w = 0$. Like in the related triple-perovskite-type $YBa_2Fe_3O_{8+w}$, the added oxygen atoms w are accommodated in the RE layer. The homogeneity range in w is very wide, extending from 0.02(1) for RE = Sm and 0.050(6) for RE = Nd to $w = 0.65$ and $w = 0.80$, respectively, seen in O_2 at 985 °C without the upper homogeneity limit being crossed. The most reduced $REBaFe_2O_{5+w}$ phases oxidize very easily, even at room temperature. The crystal structure, as seen at room temperature after quenching from *ca.* 1000 °C, is tetragonal, except for the most reduced compositions for RE = Sm ($w < 0.045$) and most oxidized compositions for RE = Nd ($w = 0.69$ as an example) which are orthorhombic. For samples with $w = 0.5$ low temperature (*ca.* 500 °C) annealing leads to ordering of the added oxygens within the rare earth layer. This ordering produces equal concentrations of square pyramidal and octahedral Fe^{3+}. The ordered structure, a type which has not previously been observed, belongs to space group *Pmna* (no. 53) with $a \approx 4a_p$, $b \approx a_p$ and $c \approx 2a_p$, where a_p is the primitive cubic perovskite cell edge ($a_p \approx 3.9$ Å). Structural refinements were obtained by applying the Rietveld method to synchrotron X-ray powder diffraction data.

Introduction

Perovskite-type rare-earth (RE) alkaline-earth iron oxides have wide stability ranges where the Fe valence and oxygen content can be varied. As a result of that, these ceramic materials are good electronic conductors with significant participation of oxygen ions as charge carriers. This combination of properties is often associated with structures that possess a well ordered framework and a significant concentration of vacancies.[1] There is considerable interest in materials which show both ionic and electronic conductivity as electrode materials in batteries,[2] fuel cells[3] and as separation membranes.[4,5] One of the simplest ordering schemes for a single-perovskite cell is duplication and triplication. Both single-perovskite cubic $Ba(RE_{0.1}Fe_{0.9})O_{3-\delta}$ (RE = Y),[6,7] $(RE_{1/3}Ba_{2/3})FeO_{3-\delta}$ (RE = Nd, La)[8] and triple-perovskite $REBa_2Fe_3O_{8+\delta}$ (RE = Dy–Er, Y)[8,9] can be synthesized when RE is appropriately sized. However, the double-perovskite variant has not been reported. Such structure is formed for Mn, $REBaMn_2O_{5+\delta}$ (RE = Y),[10–12] and for combinations of some transition metals, $REBaCuFeO_5$ (RE = Y,[13] Pr[14]) and $REBaCuCoO_5$ (RE = Y).[15] In the latter group with non-uniform redox behaviour, the oxygen content cannot be varied in wide ranges.

In this communication, the synthesis of $REBaFe_2O_{5+w}$ (RE = Nd and Sm) with oxygen content varied across the large homogeneity range in w is reported and the associated variations in crystal structure are evaluated by Rietveld refinements from synchrotron powder diffraction data. This is intended as a first step to the solution of a complex combined nuclear and magnetic structures characteristic of these compounds, as revealed by neutron powder diffraction data collected on $REBaFe_2O_{5+w}$ samples.

†Present address: Department of Chemistry, Ohio State University, Newman and Wolfram Laboratory, 100 West 18th Avenue, Columbus, OH 43210–1185, USA, e-mail: woodward@chemistry.ohio-state.edu

Experimental

Syntheses

The bulk oxides were synthesized from nanoscale precursors obtained by liquid mixing in citrate melts.[16] Iron lumps (99.95%, Koch-Light) were converted to iron nitrate with dilute HNO_3 (Baker, analyzed) prior to adding to the melted citric acid monohydrate (99%, Fluka, reagent grade) into which Nd_2O_3 or Sm_2O_3 (>99.9% REs, Molycorp) already had been dissolved (1 mol of RE_2O_3 per 48 mol of citric acid). When the evolution of nitrous gases ceased, water was added and dried barium carbonate (0.1% Sr, Merck) was dissolved. The clear viscous melt, formed by the subsequent evaporation of water, was dehydrated into a solid at 180 °C, milled, and the resulting fine powder was slowly incinerated in a crucible over two days at 450 °C in air.

Thus obtained precursors were calcined in a reducing atmosphere into dark brown powders, homogenized in a vibrational agate mill, and sintered under conditions chosen to obtain fully compact samples. The calcination and sintering conditions are listed in Table 1. The sintered cylinders with a silvery luster were used for the subsequent control of the oxygen content by quenching.

Oxygen content control

Samples were obtained by quenching from equilibrium conditions defined by temperature and partial pressure of

Table 1 Temperature (t), partial pressures of oxygen and mixing volume ratios R of Ar-to-H_2 in the flowing atmosphere and times of calcination and sintering (τ) for $REBaFe_2O_{5+w}$

RE/process	t/°C	log (p_{O_2}/bar)	R^a	τ/h
Nd/calcination	930	−16.0	30	16
Nd/sintering	1040	−15.2	10	120
Sm/calcination	900	−16.6	30	16
Sm/sintering	985	−15.5	20	120

[a]Saturated by water vapour to $p_{H_2O} \approx 0.018$ bar.

oxygen. The atmosphere composition was controlled by mixing of argon, hydrogen or oxygen (all 99.999%) and water vapour, the latter being introduced from a saturator containing *ca.* 45 wt.% solution of H_3PO_4 of known concentration and temperature. The partial pressures of oxygen were calculated from the dilution ratios and thermodynamic data[17,18] for the formation of H_2O. The samples, contained in a closed-end corundum tube, were placed inside a vertical tube furnace and heated to 985 °C for 120 h. They were then quenched by lowering the closed-end corundum tube from the furnace. The quench rate corresponds to some 2 min to the disappearance of the red glow, and this was considered sufficient considering that the samples were completely compact.

Oxygen content analyses

The oxygen content of all samples was determined cerimetrically. Powdered samples (*ca.* 0.15 g) were dissolved in 6 mL water and 3 mL concentrated HCl in a 10 mL ampoule sealed under Ar. In cases when divalent iron was not present in the sample, a specified amount of the Mohr's salt was added and the amount of HCl doubled at the expense of water. The dissolutions (aided by an ultrasound stirring and temperatures of 50–60 °C) lasted some 5 min. The resulting solutions were complexed with 10 mL of concentrated phosphoric acid and titrated at room temperature under Ar with ferroin as an indicator. Each determination was performed in duplicate or triplicate. The estimated standard deviations of the w values did not exceed 0.003.

Conventional powder X-ray diffraction

The phase purity and unit-cell parameters of all samples were evaluated from powder X-ray diffraction (PXD) data obtained with a Guinier–Hägg camera with Cu-Kα_1 radiation and Si as an internal standard. The photographs were scanned by an LS-18 film scanner with software by Werner[19] for further X-ray data treatment.

Synchrotron powder X-ray diffraction

Diffraction data for selected samples were collected on the X7A beamline at the National Synchrotron Light Source (NSLS) located at Brookhaven National Laboratory (BNL). Monochromatic radiation ($\lambda = 0.7012$ Å) was obtained from a channel-cut double crystal Si(111) monochromator. The multiwire linear position-sensitive detector filled with Kr collects 4° of data (in 2θ) at each step of 0.25° so that there is a considerable overlap in the data collected at each step. Local software is used to merge these data into a single pattern with a step size of 0.01° in 2θ. This step value was chosen so that at minimum three to five points are available to span the FWHM of the sharpest peaks. Collecting and processing the data in this way results in an effective collection time of 16 × the count time at each point (this results in extremely good statistics, which paradoxically causes the $\chi^2 = R_{wp}{}^2/R_{exp}{}^2$ values to be high due to the very low R_{exp}). Patterns were collected over the angular range of $4 < 2\theta < 64°$ with counting times increasing from 20 s per step for the low-angle region to 60 s per step for the high-angle region. The count times were doubled and the angular range extended to 76° for data collections with the ordered $w = 0.5$ samples. The samples were filled in glass capillaries of diameter between 0.25 and 0.36 and rotated during the data collection. The apparent sample density was estimated by weighing the empty and filled capillary, and applying the absorption correction for a cylindrical sample[20] in the refinements. Since the μR values were not too high (between 1 and 1.5) the empirical formula according to Hewat[21] and Rouse, Cooper and Chakera[22] was adopted for this angle-dependent correction. Structural refinements were performed using the Rietveld method as implemented in the GSAS software suite, written by Allen Larson and Robert Von Dreele. In addition to the absorption correction mentioned above, corrections for anomalous dispersion were also made. A linear interpolation between fixed points was used to model the background. GSAS's pseudo-Voigt function is used to model the peaks, in general, Lorentzian coefficients X and Y eventually complemented by the U and W Gaussian coefficients (the samples were quenched), together with coefficients for the sample asymmetry and shift and for the anisotropy of the principal (Lorentzian Scherrer) broadening.

Results

Formation and characterizations

The sintered master samples of $REBaFe_2O_{5+w}$ (RE = Nd and Sm; $w \approx 0.1$) were single phase, isostructural with $YBaCuFeO_5$,[23] $YBaCuCoO_5$[24] and $YBaMn_2O_5$.[10] Under present synthesis conditions, $REBaFe_2O_{5+w}$ is formed also for RE = Gd, as an example, but not for RE = La (which gives a cubic perovskite-type phase instead) and Y (which gives a mixture of $YBa_2Fe_3O_8$ and $YFeO_3$ instead). A glimpse into the phase diagram of $REBaFe_2O_{5+w}$ in reducing environments has been obtained with trial compositions 113 and 123 (referring to RE, Ba and Fe), and is presented in Table 2 for $NdBaFe_2O_{5+w}$. The coexistent phases illustrate the stability of these double-perovskite-type iron oxides under reducing conditions. The title oxides are stable also under relatively high partial pressures of oxygen, as reflected in the broad range of non-stoichiometry for samples quenched from high temperatures (around 1000 °C). However, for a special composition of $w = 0.5$, a complete ordering of the added oxygens w (a $RE_2Ba_2Fe_4O_{11}$ superstructure) is observed at lower temperatures (700 and 500 °C tested).

The composition limits for the double-perovskite-type $REBaFe_2O_{5+w}$ are somewhat different for RE = Nd and Sm. For RE = Nd, the oxygen content could be varied from $w = 0.050(6)$, which is the lower decomposition limit at 1040 °C, up to $w = 0.792(1)$ obtained in pure O_2 at 985 °C without crossing the upper homogeneity limit. For RE = Sm, the lower decomposition limit is $w = 0.02(1)$ at 985 °C, and $w = 0.646(2)$ is obtained in pure O_2 at the same temperature without decomposition. However, the accommodation of such amounts of added oxygen is not without consequences for structural or compositional stabilities. A structural instability is seen for the quenched (985 °C) $NdBaFe_2O_{5.50}$ sample in which a portion (16 wt.%) of the ordered superstructure phase $Nd_2Ba_2Fe_4O_{11}$ is identified in the synchrotron PXD patterns. Analogous Sm sample develops a compositional instability instead, and Rietveld refinements revealed a presence of 25 wt.% of a cubic perovskite-type $(Sm,Ba)FeO_{3-\delta}$. In addition to this, a small admixture of 1–5 wt.% of $SmFeO_3$ is seen for $w \geqslant 0.300$, but no apparent admixtures occur in the more reduced samples.

Strong sintering in reducing atmospheres is observed under conditions listed in Table 1, and experiments under equilibrium partial pressures of oxygen show that this is associated with a

Table 2 A glimpse of the phase diagram: some two-phase compatibilities of $NdBaFe_2O_{5+w}$ under reducing conditions at 1040 °C

Overall[a]	w[b]	Second phase	$\log(p_{O_2}/\text{bar})$
113	5.07	Fe	−15.6
123	5.10	$Ba_{0.9}Nd_{0.1}FeO_{2.50}$[c]	−14.4
113	5.29	FeO	−13.4
113	5.30	Fe_3O_4	−12.4

[a]A shorthand for the overall composition referring to the metals ratio. [b]In the $NdBaFe_2O_{5+w}$ phase; by Vegard rule. [c]$a = 4.0293(2)$ Å; composition balances: metals from the phase content, oxygen content from the overall oxygen content.

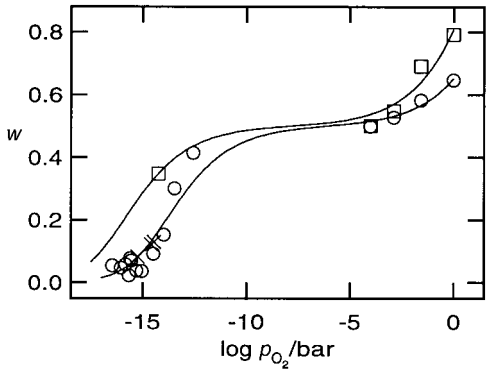

Fig. 1 Quenching conditions of $REBaFe_2O_{5+w}$ at 985 °C. RE = Nd (□) and Sm (○), the Nd samples quenched from 1040 °C are marked by crosses.

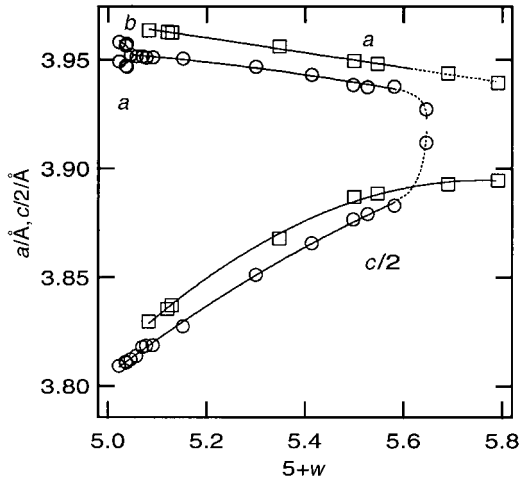

Fig. 2 Unit-cell parameters of synthesized $REBaFe_2O_{5+w}$ samples as a function of w, evaluated from Guinier–Hägg camera photographs. RE = Nd (□) and Sm (○), the size of the symbols is at least five times the standard deviations along both axes. Lines are fitted as guides for the eye, ranges with poorly resolved structural distortions are dotted.

decrease in the temperature of melting with decreasing w. The same behaviour is observed[25] for $YBa_2Fe_3O_{8+w'}$, except that the present materials $REBaFe_2O_{5+w}$ tolerate stronger reducing conditions both in terms of temperature and partial pressures of oxygen. The sintered, most reduced and most oxidized samples are silvery black, but under oxygen partial pressures around $p_{O_2} = 10^{-5}$ bar (established in Ar-rich mixtures) the samples acquire the red colour typical of trivalent iron.

The conditions controlling the oxygen-content of the samples have been checked for consistency using a simple model based on point-defects and oxygen equilibrium conditions. $REBaFe_2O_{5+w}$ is treated as stoichiometric when all iron is trivalent ($w = 0.5$). The RE atoms are defined as single-electron donor dopants, since they have one more valence electron than Ba. These assumptions define the lower limit of the oxygen content to be 5 per formula unit. The defect system is then dominated by oxygen interstitials (oxygen vacancies are neglected) which participate in the oxygen exchange with the flowing gas: $O_2 \rightleftharpoons 4h^{\cdot} + 2O''_i$ and $2O''_i \rightleftharpoons 4e' + O_2$. Concentrations are constrained by the electroneutrality condition: $[e'] + 2[O''_i] = [h^{\cdot}] + [RE^{\cdot}_{Ba}]$. Combining this expression with equilibrium constants for the two oxygen-exchange reactions above, w can be expressed as a function of $\log p_{O_2}$. This relationship is then used to fit the experimental data in Fig. 1. It is seen that no coarse inconsistencies occur among oxygen contents of the samples and the quenching conditions, and a reasonable agreement is obtained also with the simple defect model.

The $REBaFe_2O_{5+w}$ samples which contain divalent iron oxidize easily under non-equilibrium conditions, both on the side of the higher partial pressures of oxygen and lower temperatures and this even includes room temperature. As an example, the powder crushed by a pestle and mortar from the completely sintered samples oxidizes in air at the rate of some 0.01 in units of w per week. Therefore, the samples were kept under a protecting Ar atmosphere, and eventually sealed in small glass ampoules.

Crystal structures

Disordered high-temperature variants. A centrosymmetric model has been adopted for the ideal prototype structure of $REBaFe_2O_5$. This is based on neutron powder diffraction results for $REBaFeCuO_5$[26] and $REBaFeCoO_5$[24] suggesting that the di- and tri-valent metal atoms are disordered over one crystallographic site in square-pyramidal coordination. However, $REBaFe_2O_{5+w}$ has several features which go over this simple model: (i) a wide homogeneity range in w. The only site available for the added oxygen atoms w is at the bases of the coordination pyramids. (ii) A minor orthorhombic deformation, observed close to the homogeneity limits (Fig. 2). This occurs for $SmBaFe_2O_{5+w}$ in the vicinity of the lower end ($w < 0.045$) and for $NdBaFe_2O_{5+w}$ in the vicinity of the upper end of the homogeneity range (the latter distinguished well only in the synchrotron PXD patterns). (iii) Compositions with high w must maintain the added oxygen atoms (w) in randomly distributed state. The only synthesis route is quenching and the occurring instabilities involve precipitation of *structurally related* ordered or otherwise related perovskite-type phases.

In line with this, structural refinements gave very good results for low values of w, whereas modelling of the structural effects was difficult when large proportions of the added oxygens were present. In the end, the simplest model has been adopted, across the entire homogeneity ranges, which introduces a split Fe position in proportion to the added oxygens w. In this split position, the 'octahedral' portion of Fe is fixed at $z = 1/4$ whereas the 'square-pyramidal' portion of Fe is free for refinement. This model is illustrated in Fig. 3.

Judging from the ordered structure (see the following section), where all variables were fully refined, this may not be a completely accurate assumption for the samples with high w, but rather a reasonable approximation to the average of the true local environments. Mössbauer analysis of related oxides shows that similar environments involve a statistical distribution of coordination polyhedra with $CN \leqslant 6$, as well as of several valence and spin states of iron.[27] This calls either for an accurate modelling of the occurring disorder, or for a series of approximations. Since the disorder concerns mainly oxygen atoms which have low scattering factors as compared

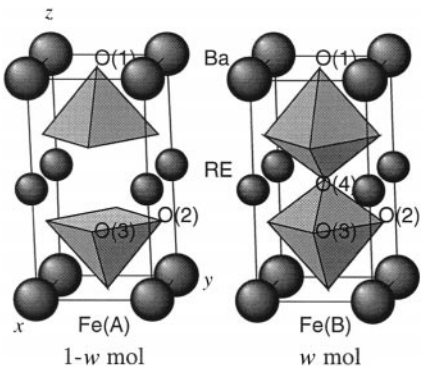

Fig. 3 General structure model for disordered double-perovskite-type $REBaFe_2O_{5+w}$ as used in Rietveld refinements. Orthorhombic labelling is shown; in tetragonal versions O(2) and O(3) sites merge into O(23).

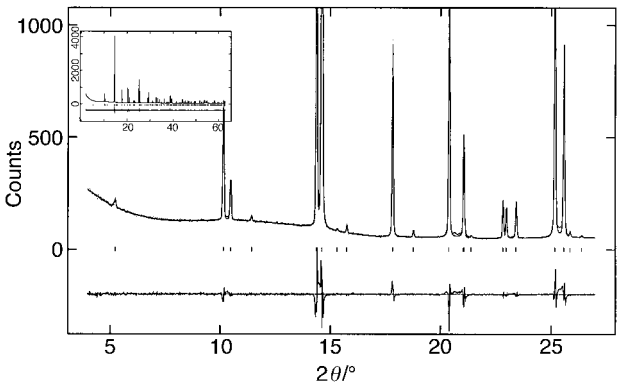

Fig. 4 Detail of the observed, calculated and difference pattern from Rietveld refinement of $NdBaFe_2O_{5.129}$. The entire pattern is in the insert. The background elevation is due to the glass capillary.

with the other atoms present, the accurate modelling proved not possible. In the final refinements of all high-temperature disordered samples, temperature factors were constrained equal for all oxygens, for Ba and the RE atom present, and for Fe(A) and Fe(B). Occupancies were fixed according to the model in Fig. 3 corresponding to the cerimetric oxygen content. The main reasons for the constraints implemented are presented in the following paragraph.

In the course of refinements of the high-w samples, a release of z parameters for the 'octahedral' and 'square-pyramidal' iron was not stable. On the other hand, having only one single iron site tended to give unrealistically short Fe–O(4) distances. An attempt to model the statistical disorder of coordinations *via* oxygen occupancies constrained in terms of a partial structural disproportionation of square pyramids into squares and octahedra was not systematically refinable for all samples. Neither a simplification of this disorder *via* introduction of a split O(23) site, as in a neutron diffraction study of a similar oxide,[28] was supported by the data. Refinements of completely unconstrained oxygen occupancies (with temperature factors constrained equal) essentially confirmed the content of the added oxygens (w) at the O(4) site (differences of some 0.05 at most), and gave somewhat lower values than 1.0 for the O(1) and O(23) occupancies (a difference between 0.05 and 0.1). A subsequent release of the oxygen temperature factors resulted in their unrealistic values with unsystematic variations from sample to sample. Also the oxygen occupancies become less reasonable. Importantly, however, none of this affected the atomic coordinates in an extent that exceeded their standard deviations, and improvements in figures of merits were at best marginal. The high thermal factors were also rather independent of the modelling of the Fe site (a split, anisotropy). For one sample ($NdBaFe_2O_{5.50}$), a negative temperature factor is obtained for Fe. It seems that this particular problem is caused by the fact that, under quenching, a portion of a partially ordered $Nd_2Ba_2Fe_4O_{11}$ phase was formed, the ordering degree of which is difficult to model.

In general, the refined structural parameters confirm the basic structural model for the high-temperature (disordered) variants of $REBaFe_2O_{5+w}$, having the duplicate perovskite-type structure and a partial occupancy at the site which accommodates the added oxygens w. In order to illustrate the good fits to the lowest-intensity peaks, a section is cut and enlarged from the low-angle portion of the refined pattern and shown in Fig. 4. The refined chemical-phase and unit-cell data are listed in Tables 3 and 4 and the corresponding atomic structural parameters in Tables 5 and 6.

Despite the constraints placed on the refinement, the bond distances and bond valences (Table 7; calculated according to Brown[29] with parameters by Brese and O'Keeffe[30] using linear interpolation for the variation of the iron parameter with valence) suggest that our modeling of the structure is chemically reasonable. In particular, the bond valence of Fe is in an excellent agreement with the formal valence $v(Fe)=2.5+w$. The bond valence of Ba fits very well for low w, but increases for oxidized samples, obviously due to the contraction of the *ab* plane, and this happens in both Nd and Sm variants. The bond valences of the RE atoms themselves differ somewhat. Except for the most oxidized samples, Sm is slightly underbonded (too small) and Nd slightly overbonded (too large). In the most oxidized samples with $w>0.5$, both begin to be underbonded and this must be associated with the expansion along c (due to the insertion of the added oxygens) which the newly appearing RE–O(4) bonds do not fully compensate.

Table 3 Refinement statistics, phase data, space group and unit cell parameters for $SmBaFe_2O_{5+w}$

Phase[a]	$SmBaFe_2O_{5.036(2)}$	$SmBaFe_2O_{5.091(1)}$	$SmBaFe_2O_{5.498(1)}$	$SmBaFe_2O_{5.582(2)}$
Space group	*Pmmm*	*P*4/*mmm*	*P*4/*mmm*	*P*4/*mmm*
a/Å	3.94611(3)	3.95091(2)	3.93970(2)	3.93867(2)
b/Å	3.95780(3)			
c/Å	7.62294(6)	7.64129(5)	7.75526(5)	7.76647(5)
Volume/Å^3	119.055(2)	119.278(1)	120.371(1)	120.482(1)
Wt. fraction (%)	100	100	70.0	96.8
Phase			$SmFeO_3$	$SmFeO_3$
Space group			*Pnma*	*Pnma*
a/Å			5.5910(8)	5.577(1)
b/Å			7.732(1)	7.717(1)
c/Å			5.4194(6)	5.409(1)
Volume/Å^3			234.28(5)	232.80(7)
Wt. fraction			5.3	3.2
Phase			(Sm,Ba)FeO_3[b]	
Space group			*Pm*$\bar{3}$*m*	
a/Å			3.94246(5)	
Volume/Å^3			61.277(1)	
Wt. fraction			24.7	
R_{wp} (%)	5.29	4.97	4.81	5.97
R_p (%)	3.31	3.27	3.06	3.99
R_{F^2} (%)	3.87	4.23	4.21	4.57
χ^2	15.56	9.96	14.39	27.06
N_{obs}	341	180	760	711
No. of variables	16	16	24	19

[a]Cerimetric oxygen-content, estimated standard deviations in parentheses. [b]Sm : Ba fixed arbitrarily to 1 : 1.

Table 4 Refinement statistics, phase data, space group and unit cell parameters for $NdBaFe_2O_{5+w}$

Phase[a]	$NdBaFe_2O_{5.129(1)}$	$NdBaFe_2O_{5.500(2)}$	$NdBaFe_2O_{5.690(2)}$
Space group	*P*4/*mmm*	*P*4/*mmm*	*Pmmm*
a/Å	3.96204(2)	3.94992(1)	3.93723(3)
b/Å			3.94830(3)
c/Å	7.67731(6)	7.77414(3)	7.78524(4)
Volume/Å^3	120.517(1)	121.291(1)	121.025(1)
Wt. fraction	100	85.5	100
Phase		$Nd_2Ba_2Fe_4O_{11}$	
Space group		*Pmna*	
a/Å		15.5510(8)	
b/Å		3.9212(2)	
c/Å		7.9520(4)	
Volume/Å^3		484.90(4)	
Wt. fraction		14.5	
R_{wp} (%)	5.88	4.34	5.79
R_p (%)	3.62	2.85	3.42
R_{F^2} (%)	4.00	6.79	4.59
χ^2	14.35	11.48	17.3
N_{obs}	173	1239	342
No. of variables	16	27	16

[a]Cerimetric oxygen-content, estimated standard deviations in parentheses.

Table 5 $SmBaFe_2O_{5+w}$ refined atomic coordinates, temperature factors (U_{iso}) and fixed occupancies *n*. Standard deviations for *fitted* variables are in parentheses

$w=0.036$	*Pmmm*	*x*	*y*	*z*	$100U_{iso}$/Å^2	*n*
Sm	1*c*	0	0	0.5	0.670(8)	1
Ba	1*a*	0	0	0	0.670(8)	1
Fe(A)	2*t*	0.5	0.5	0.2629(2)	0.52(2)	0.964
Fe(B)	2*t*	0.5	0.5	0.25	0.52(2)	0.036
O(1)	1*f*	0.5	0.5	0	1.22(7)	1
O(2)	2*s*	0.5	0	0.3042(13)	1.22(7)	1
O(3)	2*r*	0	0.5	0.3095(13)	1.22(7)	1
O(4)	1*h*	0.5	0.5	0.5	1.22(7)	0.036
$w=0.091$	*P*4/*mmm*					*n*
Sm	1*b*	0	0	0.5	0.260(7)	1
Ba	1*a*	0	0	0	0.260(7)	1
Fe(A)	2*h*	0.5	0.5	0.2628(2)	0.445(18)	0.909
Fe(B)	2*h*	0.5	0.5	0.25	0.445(18)	0.091
O(1)	1*c*	0.5	0.5	0	0.67(6)	1
O(23)	4*i*	0.5	0	0.3058(4)	0.67(6)	1
O(4)	1*d*	0.5	0.5	0.5	0.67(6)	0.091
$w=0.498$	*P*4/*mmm*					n^a
Sm	1*b*	0	0	0.5	0.907(11)	1
Ba	1*a*	0	0	0	0.907(11)	1
Fe(A)	2*h*	0.5	0.5	0.2567(7)	0.087(19)	0.50
Fe(B)	2*h*	0.5	0.5	0.25	0.087(19)	0.50
O(1)	1*c*	0.5	0.5	0	3.29(11)	1
O(23)	4*i*	0.5	0	0.2909(6)	3.29(11)	1
O(4)	1*d*	0.5	0.5	0.5	3.29(11)	0.50
$w=0.582$	*P*4/*mmm*					n^a
Sm	1*b*	0	0	0.5	0.934(8)	1
Ba	1*a*	0	0	0	0.934(8)	1
Fe(A)	2*h*	0.5	0.5	0.2567(7)	0.251(17)	0.42
Fe(B)	2*h*	0.5	0.5	0.25	0.251(17)	0.58
O(1)	1*c*	0.5	0.5	0	2.48(8)	1
O(23)	4*i*	0.5	0	0.2874(5)	2.48(8)	1
O(4)	1*d*	0.5	0.5	0.5	2.48(8)	0.58

[a]Effect of the minor $SmFeO_3$-type phase on the composition of the major phase is neglected.

Table 6 $NdBaFe_2O_{5+w}$ refined atomic coordinates, temperature factors (U_{iso}) and fixed occupancies *n*. Standard deviations for *fitted* variables are in parentheses

$w=0.129$	*P*4/*mmm*	*x*	*y*	*z*	$100U_{iso}$/Å^2	*n*
Nd	1*b*	0	0	0.5	0.376(9)	1
Ba	1*a*	0	0	0	0.376(9)	1
Fe(A)	2*h*	0.5	0.5	0.2599(4)	0.140(29)	0.87
Fe(B)	2*h*	0.5	0.5	0.25	0.140(22)	0.13
O(1)	1*c*	0.5	0.5	0	0.77(9)	1
O(23)	4*i*	0	0.5	0.3019(5)	0.77(9)	1
O(4)	1*d*	0.5	0.5	0.5	0.77(9)	1.13
$w=0.500$	*P*4/*mmm*					
Nd	1*b*	0	0	0.5	0.505(8)	1
Ba	1*a*	0	0	0	0.505(8)	1
Fe(A)	2*h*	0.5	0.5	0.2513(7)	−0.09(1)	0.50
Fe(B)	2*h*	0.5	0.5	0.25	−0.09(1)	0.50
O(1)	1*c*	0.5	0.5	0	1.07(6)	1
O(23)	4*i*	0	0.5	0.2913(4)	1.07(6)	1
O(4)	1*d*	0.5	0.5	0.5	1.07(6)	0.50
$w=0.690$	*Pmmm*					
Nd	1*c*	0	0	0.5	0.544(7)	1
Ba	1*a*	0	0	0	0.544(7)	1
Fe(A)	2*t*	0.5	0.5	0.2550(12)	0.138(15)	0.31
Fe(B)	2*t*	0.5	0.5	0.25	0.138(15)	0.69
O(1)	1*f*	0.5	0.5	0	1.41(6)	1
O(2)	2*s*	0.5	0	0.2860(12)	1.41(6)	1
O(3)	2*r*	0	0.5	0.2830(13)	1.41(6)	1
O(4)	1*h*	0.5	0.5	0.5	1.41(6)	0.69

Ordered low-temperature variants. The ordered $REBaFe_2O_{5.50}$ PXD patterns develop *via* an orthorhombic deformation of the tetragonal prototype followed by a doubling of two axes: the *c* axis and the longer of the two axes created by the orthorhombic distortion (*a*). Weak 'superstructure' lines appear in the low-angle portion of the PXD diagram (see Fig. 5). The systematic absences are then consistent with nonstandard space groups *Pcnm* (no. 53) and *Pcn*2 (no. 30); in standard setting *Pmna* (no. 53) and *P*2*na* (no. 30). Refinements in the higher symmetry space group *Pmna* resulted in an excellent fit to the data, therefore, the lower symmetry non-centrosymmetric space group was rejected. Refinement details are listed in Table 8, fractional coordinates and thermal parameters are tabulated in Table 9, bond valences and selected bond distances are listed in Table 10.

The structure of $Nd_2Ba_2Fe_4O_{11}$ is shown in Fig. 6. The ordered distribution of the square-pyramidal and octahedral iron is evident in this figure. The bond valences in Table 10 show that even though the two iron sites have different coordination environments the distribution of Fe–O distances about each site is consistent with trivalent iron. This is achieved primarily by a shift in the O(1) position toward square-

Table 7 Selected interatomic distances (Å) and bond valences BV for 'disordered' double-perovskite $REBaFe_2O_{5+w}$

	$SmBaFe_2O_{5.036}$	$SmBaFe_2O_{5.091}$	$SmBaFe_2O_{5.498}$	$SmBaFe_2O_{5.582}$	$NdBaFe_2O_{5.129}$	$NdBaFe_2O_{5.500}$	$NdBaFe_2O_{5.690}$
Fe(A)–O(1)	2.004(2)	2.008(2)	1.991(5)	1.994(6)	1.996(3)	1.954(5)	1.985(9)
Fe(A)–O(2)	2.004(2)	2.003(1)	1.988(1)	1.984(1)	2.007(1)	1.999(1)	1.989(2)
Fe(A)–O(3)	2.005(2)						1.981(2)
Fe(B)–O(1)	1.9057	1.9103	1.9388	1.9416	1.9193	1.9435	1.9463
Fe(B)–O(2)	2.022(2)	2.0209(6)	1.9952(7)	1.9906(6)	2.0207(9)	2.0009(5)	1.994(1)
Fe(B)–O(3)	2.024(2)						1.985(1)
Fe(B)–O(4)	1.9057	1.9103	1.9388	1.9416	1.9193	1.9435	1.9463
Ba–O(1)	2.7945	2.7937	2.7858	2.7851	2.8016	2.7930	2.7880
Ba–O(2)	3.045(8)	3.060(2)	2.995(4)	2.977(3)	3.049(4)	3.005(4)	2.972(7)
Ba–O(3)	3.079(8)						2.958(8)
RE–O(2)	2.474(6)	2.471(2)	2.552(3)	2.570(2)	2.498(3)	2.556(2)	2.579(6)
RE–O(3)	2.455(6)						2.598(7)
RE–O(4)	2.7945	2.7937	2.7858	2.7851	2.8016	2.7930	2.7880
O(1)–O(2)	3.048(8)	3.060(2)	2.995(4)	2.977(3)	3.049(4)	3.005(2)	2.976(7)
O(1)–O(3)	3.076(8)						2.955(8)
O(4)–O(2)	2.479(6)	2.471(2)	2.552(3)	2.570(2)	2.498(3)	2.556(2)	2.583(6)
O(4)–O(3)	2.450(6)						2.594(7)
BV_{Fe}	2.52(3)	2.57(4)	3.05(5)	3.09(5)	2.59(4)	2.98(5)	3.18(6)
BV_{Ba}	1.99(2)	1.997(6)	2.21(1)	2.27(1)	2.00(1)	2.16(1)	2.30(2)
BV_{RE}	2.92(5)	2.95(1)	2.95(2)	2.88(1)	3.02(2)	3.09(1)	2.69(4)

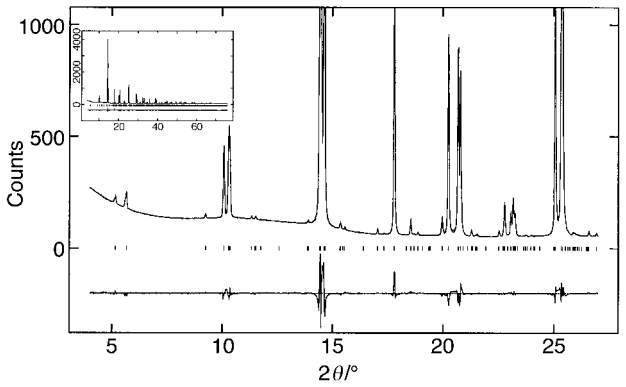

Fig. 5 Enlarged detail of the observed, calculated and difference pattern from Rietveld refinement of $Nd_2Ba_2Fe_4O_{11}$. The entire pattern is in the insert. The background elevation is due to the glass capillary.

Table 8 Refinement statistics, phase data, space group and unit cell parameters for ordered $RE_2Ba_2Fe_4O_{11}$ (RE = Nd, Sm)

Phase	$Nd_2Ba_2Fe_4O_{11}$	$Sm_2Ba_2Fe_4O_{11}$
Space group	*Pmna*	*Pmna*
a/Å	15.54166(8)	15.47744(7)
b/Å	3.90558(2)	3.89602(2)
c/Å	7.97730(4)	7.96825(3)
Volume/Å^3	484.215(4)	480.489(4)
Wt. fraction (%)	100	88
Phase		$SmBaFe_2O_{5.50}$
Space group		*P*4/*mmm*
a/Å		3.9379(1)
c/Å		7.7408(4)
Volume/Å^3		120.038(6)
Wt. fraction		12[a]
R_{wp} (%)	4.48	4.32
R_p (%)	3.01	2.86
R_{F^2} (%)	4.69	4.10
χ^2	12.3	16.5
N_{obs}	1498	1747
No. of variables	30	32

[a]A very small amount of an unidentified phase is also present.

pyramidal Fe(1). Consequently, unlike the situation for small values of *w* where the square pyramids are fairly regular, both the octahedra and the square pyramids are highly distorted in the ordered structure. Another difference between the ordered structures and those corresponding to $w \approx 0$, is that in the latter case the bond valences for both barium and the rare earth ion are near their ideal values, whereas in the former case Ba is overbonded and Nd/Sm is underbonded. This is reflecting the structurally destabilizing influence of the 'excess' oxygen.

Table 9 Ordered $RE_2Ba_2Fe_4O_{11}$ (RE = Nd, Sm) refined atomic coordinates, temperature factors (U_{iso}) and occupancies *n*. Standard deviations for *fitted* variables are in parentheses

Atom	Site	*x*	*y*	*z*	$100U_{iso}$[a]/Å^2	*n*
Ba	4*g*	0.75	0.509(1)	0.25	0.21(3)	1
Nd	4*h*	0.0	0.503(2)	0.2669(1)	0.21(3)	1
Fe(1)	4*e*	0.8739(3)	0.0	0.0	−0.09(5)	1
Fe(2)	4*e*	0.6237(3)	0.0	0.0	−0.07(5)	1
O(1)	8*i*	0.8948(3)	−0.022(4)	0.2378(8)	0.4(2)	1
O(2)	4*f*	0.9076(5)	0.5	0.0	0.4(2)	1
O(3)	4*f*	0.620(1)	0.5	0.0	0.4(2)	1
O(4)	4*e*	0.7538(9)	0.0	0.0	0.0(1)	1
O(5)	2*b*	0.0	0.0	0.5	0.0(1)	1
Ba	4*g*	0.75	0.499(2)	0.25	0.30(3)	1
Sm	4*h*	0.0	0.501(2)	0.2651(1)	0.31(3)	1
Fe(1)	4*e*	0.8751(3)	0.0	0.0	0.10(2)	1
Fe(2)	4*e*	0.6229(3)	0.0	0.0	0.10(2)	1
O(1)	8*i*	0.8977(3)	−0.044(2)	0.2383(9)	0.0(2)	1
O(2)	4*f*	0.9091(6)	0.5	0.0	1.7(2)	1
O(3)	4*f*	0.626(1)	0.5	0.0	1.7(2)	1
O(4)	4*e*	0.753(1)	0.0	0.0	0.8(1)	1
O(5)	2*b*	0.0	0.0	0.5	0.8(1)	1

[a]Constrained equal for O(2),O(3) and O(4)/O(5).

Discussion

A wide variety of structural motifs are encountered in complex oxide materials. Among these the perovskite framework is undoubtedly one of the most important and frequently occurring. The ideal perovskite structure has stoichiometry AMO_3. The M-site cation is octahedrally coordinated by oxygen and the MO_6 octahedra are infinitely corner linked in three dimensions to form the structural framework (ReO_3 structure). The A-site cation sits in the center of a cube defined by eight corner linked MO_6 octahedra, and is coordinated by 12 equidistant oxygen ions in the ideal cubic structure.

Structural distortions and non-stoichiometry are commonly observed in perovskites. Structural distortions include tilting of the octahedra,[32–34] as in $GdFeO_3$,[35] distortions of the octahedra due to electronic effects, as in $LaMnO_3$,[36] and

Table 10 Selected bond distances (Å) and bond valences, BV,[a] for ordered $Nd_2Ba_2Fe_4O_{11}$ and $Sm_2Ba_2Fe_4O_{11}$

Atom	Ba	Nd	Fe(1)	Fe(2)	Oxygen BV
O(1)	2×2.90(1)	2×2.48(1)	2×1.927(6)	2×2.113(7)	1.95
	2×3.06(1)	2×2.63(1)			
O(2)	2×3.159(6)	2×2.568(5)	2×2.022(2)		1.77
O(3)	2×2.84(1)	2×2.63(1)		2×1.954(1)	2.13
O(4)	2×2.770(4)		1×1.867(1)	1×2.02(1)	2.27
	2×2.815(4)				
O(5)		1×2.688(4)		1×1.922(4)	2.12
		1×2.705(4)			
Metal BV	2.31	2.74	3.00	3.08	
Atom	Ba	Sm	Fe(1)	Fe(2)	Oxygen BV
O(1)	2×2.898(8)	2×2.388(8)	2×1.938(7)	2×2.117(7)	1.96
	2×3.117(8)	2×2.656(9)			
O(2)	2×3.168(7)	2×2.537(5)	2×2.018(3)		1.77
O(3)	2×2.76(1)	2×2.71(1)		2×1.949(1)	2.13
O(4)	2×2.785(5)		1×1.90(2)	1×2.01(2)	2.25
	2×2.788(5)				
O(5)		1×2.703(4)		1×1.902(4)	2.12
		1×2.700(4)			
Metal BV	2.38	2.68	2.93	3.08	

[a]All calculations were performed using the program Eutax.[31]

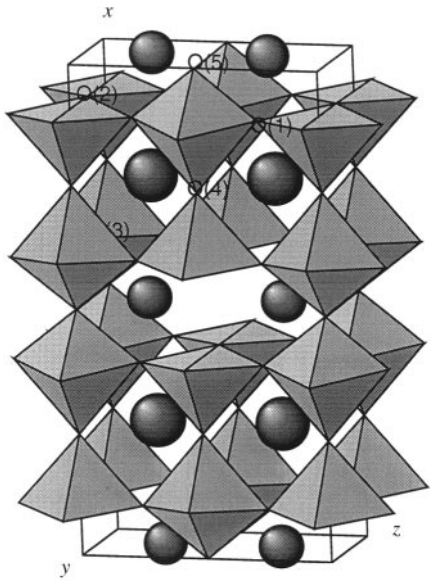

Fig. 6 Unit cell of the ordered crystal structure of $RE_2Ba_2Fe_4O_{11}$ with Fe(1) square pyramids and Fe(2) octahedra fully drawn. RE and Ba are marked as smaller and larger spheres, respectively.

ferroelectric/antiferroelectric shifts of the ions, as in $BaTiO_3$[37] and $PbZrO_3$.[38] Depending upon the composition and synthesis conditions, vacancies can be stabilized on either the cation or anion sites, and can be either ordered or disordered.

However, simple linear multiplets *m* of the single-perovskite AMO_3 cell are derived by ordering rather than distortions. Considering for simplicity only one kind of M atoms, such ordering may concern the A site and/or the eventual oxygen vacancies. Ordering of two types of A atoms (A and A′) in a 1:1 ratio will duplicate the cell, whereas the ordering in a 1:2 ratio will cause triplication. (Note that the latter could also arise from three types of A atoms.) Inserting *one* oxygen vacancy into every *m*th cell may lead to such multiplication in two different ways: (i) by interrupting the octahedral connectivity upon formation of two square pyramids, (ii) by creating two kinds of coordination polyhedra which order in a 1:1 ratio (duplication) or 1:2 ratio (triplication) while maintaining their linear connectivity. When *i* oxygen vacancies are introduced per every *m*th cell, situations like the above or none of those may occur, depending on *i* and *m*. Table 11 shows several of the ordering combinations, expressed in terms of the resulting coordination numbers of the M atoms in *m* subsequent single-perovskite subcells.

Only a few such combinations have actually been observed. The best known examples are 'triple-perovskites' with a 1:2 A-site ordering: $YBa_2Cu_3O_6$ (the 5+2+5 type in Table 11) $YBa_2Cu_3O_7$ (5+4+5) $YBa_2Fe_3O_8$ (5+6+5). 'Double-perovskites' $REBaM_2O_5$ have a 1:1 A-site ordering, and are of the 5+5 type in Table 11. These compounds enjoy the synergy of two A atoms ordering, two M-polyhedra ordering (triplicate cells only) and of the linear-connectivity interruption by a square-pyramid every *m*th cell.

Without the synergy from the two ordered and different A atoms, the vacancy ordering along one crystallographic axis is not favoured. Such $A_2M_2O_5$ oxides usually order into various diagonally multiplied unit cells which suit the coordination preferences of the M atoms and give homogeneously the coordination number 10 for the A atom. As examples (for A=Ca): M=Mn forms a $\sqrt{2}a_p$, $2\sqrt{2}a_p$, a_p-type ordering[39] M=Fe a $4a_p$, $\sqrt{2}a_p$, $\sqrt{2}a_p$-type ordering,[40] whereas M=Co has a $2\sqrt{2}a_p$, $2\sqrt{2}a_p$, $2a_p$-type ordering[41] (a_p is the 'single-perovskite' cubic cell edge).

The ordering of the A atoms alone (*viz.*, without oxygen vacancies being present) is also rare in perovskite-type oxides. Examples of such ordering include $AgNdTi_2O_6$[42] and $Na_{4/3}Th_{2/3}Ti_2O_6$,[43] both of which form a partially ordered double-perovskite-type structure.

The scarcity of the double- and triple-perovskite type structures among stoichiometric perovskites can be appreciated when the bond-valences and ionic sizes are considered. The occurrence of the terminal square-pyramid instead of an

Table 11 Combinations of coordination numbers of M[a] that duplicate (*m*=2) and triplicate (*m*=3) the single-perovskite $AMO_{3-(i/m)}$ cell[b]

	i=1	*i*=2	*i*=3
m=2	5+5		3+3
	6+4	6+2	4+2
m=3	5+6+5	5+4+5	5+2+5
	6+4+6	4+6+4	

[a]Linear connectivity within the multiple cell implies that the four-coordinated M forms a square. [b]Combinations that cannot lead to multiple cells or involve three different polyhedra are not listed.

octahedron decreases the coordination number of the adjacent A atom from 12 (cubooctahedron) to 8 (square prism). This collapse of the oxygen coordination (along the *c* axis) defines this location as the site for the smaller of the two A atoms. Since the *ab* dimensions are fixed by the size of the larger A atom, there is only a narrow bond-valence window for this smaller A′ atom (yet higher-valent than A; usually RE) to fit the square prism of oxygens. Likewise, the choice of the M atom is limited by bond valences (on top of any bond preferences due to electronic configurations) in the perovskite-type network which cannot easily deform in a cooperative manner to expand the coordination sphere about the larger A atom, contract the coordination sphere about the smaller A′ atom, and optimize the bonding interactions simultaneously.

All these double- and triple-perovskite-type structures have in common that the oxygen vacancy formation need not be fully complete, and some residual oxygen is hence allowed in the RE sphere over the coordination 8. This apparently helps to balance the bond-valence compromise (for the RE atom in particular), as different ranges in the content of these added oxygens occur for different RE. In general, the upper content of the added oxygen is expected to increase with decreasing Ba/RE size difference. In this study we observe that the most oxidized $NdBaFe_2O_{5+w}$ sample had 0.80 of the added-oxygen site filled, whereas for the smaller Sm ion only 0.65 of it could be populated. The added oxygen expands the RE coordination, leading to the increase in the *c* unit cell parameter as shown in Fig. 2. In order to compensate for this, a small contraction in the *ab* plane is observed, putting the Ba–O bonds into compression and eventually destabilizing the structure. Also in triple-perovskite-type $REBa_2Fe_3O_{8+w}$ series, the maximum *w* increases with the increasing size of the trivalent RE ion (from $w=0.07$ for RE = Er to $w=0.11$ for RE = Dy), and the increase continues even when the structure becomes disordered cubic for Gd and larger RE; up to $w=0.83$ for RE = La.[8] Two observations are interesting in this respect: (i) when the disordered cubic type is the more stable structure, even a complete removal of the added oxygens ($w\approx0$) does not cause any long-range ordering.[8] The statistics of the iron coordination polyhedra then remains random with respect to the distribution of the oxygen vacancies among the six-, five-, four-, *etc.* coordinated iron.[44] (ii) When the multiple unit cell is stable, variations in the added-oxygen content (performed at 'synthesis' temperatures to enable diffusion) do not seem to cause any disordering into the single-perovskite type. $SmBaFe_2O_{5+w}$ is closest to an exception, as the most oxidized sample with $w=0.646$ appears nearly cubic.

However, the wide range in which the added oxygen content can be varied in the title compounds brings about another type of structural instability, *viz.*, against a further ordering of the oxygen vacancies at thermodynamically favourable temperature. The composition $REBaFe_2O_{5.50}$ represents a case when one oxygen vacancy is inserted every fourth 'single-perovskite' subcell. In a first approximation, this indeed leads to a quadruplication of the cell ($m=4$), as seen along *x* in Fig. 6. But, apparently because the background ordering of RE and Ba is 1 : 1 and not 1 : 3, two such quadruplets alternate, shifted by two single-perovskite cells, to form a type of ordering so far not detected in perovskite-type oxides.

Acknowledgements

Research carried out (in part) at the National Synchrotron Light Source, Brookhaven National Laboratory, which is supported by the U.S. Department of Energy, Division of Materials Science and Division of Chemical Sciences, under contract No. DE-AC02–98CH10886.

References

1 A. Manthiram, J. F. Kuo and J. B. Goodenough, *Solid State Ionics*, 1993, **62**, 225.
2 H. Morimoto, T. Esaka and S. Takai, *Mater. Res. Bull.*, 1997, **32**, 1359.
3 J. E. Ten Elshof, M. H. R. Lankhorst and H. L. M. Bouwmeester, *J. Electrochem. Soc.*, 1997, **144**, 1060.
4 U. Balachandran, J. T. Dusek, S. M. Sweeney, R. B. Poeppel, R. L. Mieville, P. S. Maiya, M. S. Kleefisch, S. Pei, T. Kobylinski, C. A. Udovich and A. C. Bose, *Am. Ceram. Soc. Bull.*, 1995, **74**, 71.
5 S. Guggilla and A. Manthiram, *J. Electrochem. Soc.*, 1997, **144**, L120.
6 M. Parras, E. García, J. M. González-Calbet and M. Vallet-Regí, *J. Less-Common Met.*, 1991, **169**, 25.
7 P. Karen, P. H. Andresen and A. Kjekshus, *J. Solid State Chem.*, 1992, **101**, 48.
8 P. Karen, A. Kjekshus, Q. Huang, J. W. Lynn, N. Rosov, I. Natali-Sora, V. L. Karen, A. D. Mighell and A. Santoro, *J. Solid State Chem.*, 1998, **136**, 21.
9 Q. Huang, P. Karen, V. L. Karen, A. Kjekshus, J. W. Lynn, A. D. Mighell, N. Rosov and A. Santoro, *Phys. Rev. B: Condens. Matter*, 1992, **45**, 9611.
10 J. P. Chapman, J. P. Attfield, M. Mölgg, C. M. Friend and T. P. Beales, *Angew. Chem., Int. Ed. Engl.*, 1996, **35**, 2482.
11 T. P. Beales, M. Mölgg, J. Jutson and C. M. Friend, *Phys. Status Solidi*, 1997, **161**, 271.
12 J. A. McAllister and J. P. Attfield, *J. Mater. Chem.*, 1998, **8**, 1291.
13 L. Er-Rakho, C. Michel, Ph. Lacorre and B. Raveau, *J. Solid State Chem.*, 1988, **73**, 531.
14 M. Pissas, G. Kallias, V. Psycharis, H. Gamari-Seale, D. Niarchos, A. Simopoulos and R. Sonntag, *Phys. Rev. B: Condens. Matter*, 1997, **55**, 397.
15 L. Barbey, N. Nguyen, V. Caignaert, M. Hervieu and B. Raveau, *Mater. Res. Bull.*, 1992, **27**, 295.
16 P. Karen and A. Kjekshus, *J. Am. Ceram. Soc.*, 1994, **77**, 547.
17 I. Barin and O. Knacke, *Thermochemical Properties of Inorganic Substances*, Springer, Berlin, 1973, pp. 316 and 584.
18 I. Barin, O. Knacke and O. Kubashevski, *Thermochemical Properties of Inorganic Substances*, *Supplement*, Springer, Berlin, 1977, p. 295.
19 P. E. Werner, The Computer Programme SCANPI 9, Institute of Inorganic Chemistry, University of Stockholm, Sweden, 1992.
20 E. N. Maslen, in *International Tables for Crystallography*, Kluwer Academic Publishers, Dordrecht, 1992, vol. C, p. 523.
21 A. W. Hewat, *Acta Crystallogr., Sect. A*, 1979, **35**, 248.
22 K. D. Rouse, M. J. Cooper and A. Chakera, *Acta Crystallogr., Sect. A*, 1970, **26**, 682.
23 V. Caignaert, I. Mirebeau, F. Bourée, N. Nguyen, A. Ducouret, J.-M. Greneche and B. Raveau, *J. Solid State Chem.*, 1995, **114**, 24.
24 Q. Huang, P. Karen, V. L. Karen, A. Kjekshus, J. W. Lynn, A. D. Mighell, I. Natali-Sora, N. Rosov and A. Santoro, *J. Solid State Chem.*, 1994, **108**, 80.
25 P. Karen and A. Kjekshus, *J. Solid State Chem.*, 1994, **112**, 73.
26 M. J. Ruiz-Aragón, E. Morán, U. Amador, J. L. Martínez, N. H. Andersen and H. Ehrenberg, *Phys. Rev. B: Condens. Matter*, 1998, **58**, 6291.
27 J. Lindén, A. Kjekshus, P. Karen, J. Miettinen and M. Karppinen, *J. Solid State Chem.*, 1998, **139**, 168.
28 I. Natali-Sora, Q. Huang, J. W. Lynn, N. Rosov, P. Karen, A. Kjekshus, V. L. Karen, A. D. Mighell and A. Santoro, *Phys. Rev. B: Condens. Matter*, 1994, **49**, 3465.
29 I. D. Brown, *Structure and Bonding in Crystals*, ed. M. O'Keeffe, and A. Navrotsky, New York, Academic Press, 1981, vol. 2, pp. 1–30.
30 N. E. Brese and M. O'Keeffe, *Acta Crystallogr., Sect. B*, 1991, **47**, 192.
31 M. O'Keeffe, Eutax: A Program for calculating bond valences, EMLab Software, Phoenix, AZ, USA.
32 A. M. Glazer, *Acta Crystallogr., Sect. B*, 1972, **28**, 3385.
33 P. M. Woodward, *Acta Crystallogr., Sect. B*, 1997, **53**, 32.
34 P. M. Woodward, *Acta Crystallogr., Sect. B*, 1997, **53**, 44.
35 M. Marezio, J. P. Remeika and P. D. Dernier, *Acta Crystallogr., Sect. B*, 1970, **26**, 2008.
36 J. Rodríguez-Carvajal, M. Hennion, F. Moussa, A. H. Moudden, L. Pinsard and A. Revcolevschi, *Phys. Rev. B: Condens. Matter*, 1998, **57**, 3189.

37 G. H. Kwei, A. C. Larson, S. J. L. Billinge and S.-W. Cheong, *J. Phys. Chem.*, 1993, **97**, 2368.
38 A. M. Glazer, K. Roleder and J. Dec, *Acta Crystallogr., Sect. B*, 1993, **49**, 846.
39 K. R. Poeppelmeier, M. E. Leonowicz, J. C. Scanlon, J. M. Longo and W. B. Yelon, *J. Solid State Chem.*, 1982, **45**, 71.
40 A. A. Colville, *Acta Crystallogr., Sect. B*, 1970, **26**, 1469.
41 K. Vidyasagar, J. Gopalakrishnan and C. N. R. Rao, *Inorg. Chem.*, 1984, **23**, 1206.
42 J.-H. Park, P. M. Woodward and J. B. Parise, *Chem. Mater.*, 1998, **10**, 3092.
43 R. H. Mitchell and A. R. Chakhmouradian, *J. Solid State Chem.*, 1998, **138**, 307.
44 J. Lindén, M. Lippmaa, P. Karen, A. Kjekshus and M. Karppinen, *J. Solid State Chem.*, 1998, **138**, 87.

Paper 8/09302D